

Crystal chemistry and petrologic significance of Fe³⁺-rich phlogopite from the Tapira carbonatite complex, Brazil

MARIA FRANCA BRIGATTI,¹ LUCA MEDICI,¹ EMILIO SACCANI,² AND CARMELA VACCARO²

¹Dipartimento di Scienze della Terra, via S. Eufemia 19, I-41100 Modena, Italy

²Istituto di Mineralogia, Corso Ercole I d'Este 32, I-44100 Ferrara, Italy

ABSTRACT

This contribution deals with the crystal chemistry of phlogopite and Fe³⁺-rich phlogopite from the Tapira alkaline-carbonatite complex (Brazil) to assess the petrological significance and genetic conditions of these rocks. The Tapira complex consists of a layered intrusion composed mainly of ultramafic rocks (dunite, wehrlite, clinopyroxenite, bebedourite, garnet-magnetite, perovskite-magnetite, and glimmerite) with subordinate carbonatite. The wide range of textural, optical, and crystal-chemical characteristics of phlogopite is related to the variation of f_{O_2} , a_{H_2O} , and a_{CO_2} as well as magma bulk-chemical composition during fractional crystallization. Phlogopite from alkaline-silicate rocks (ranging from dunite to bebedourite) is characterized by fairly constant Al content, moderate ⁴⁴Fe³⁺ substitution, and variable amounts of Ti. The ⁴⁴Fe³⁺ substitution, accompanied by crystals showing reverse pleochroism, increases during fractional crystallization. These features correspond to crystallization at low pressure and high f_{O_2} and a_{H_2O} in the presence of moderate saturation in Ti-bearing phases, Al₂O₃ in the magma, or both. Phlogopite from silicate-carbonatite rocks, classified as ferriphlogopite on the basis of strong reverse pleochroism related to ⁴⁴Fe³⁺ tetrahedral substitution, also presents low to very low Al, Fe²⁺, and Ti contents. These features suggest very high f_{O_2} , H₂O, and CO₂ conditions in the presence of strong saturation in Ti-bearing phases as well as very low Al₂O₃ content in the liquid.

The crystal-structure refinements of Tapira phlogopite show that Fe³⁺ substitutes for Si in tetrahedral sites; Fe distribution is completely disordered, so the resulting space group is *C2/m*. The octahedral-site composition is similar to that of phlogopite, the octahedral sites being preferentially occupied by Mg. The presence of Fe³⁺ in the tetrahedral sheet enlarges the whole structure. This enlargement is reflected by an increase in cell-edge lengths and a decrease in β -angle values. The increase in distortion of the tetrahedral ring (α angle up to $\sim 11^\circ$) is necessary for the tetrahedral and octahedral sheets to fit together.

INTRODUCTION

Members of the trioctahedral mica group, such as phlogopite and biotite, are important phases in many rocks. Crystal-chemical data are therefore important to understand the nature of the reaction involving these minerals. The occurrence of Fe³⁺-rich phlogopite showing Fe³⁺ for Si tetrahedral substitution is unusual. There have been discussions of some occurrences of Fe³⁺-rich biotite and phlogopite in metapelites (Dyar 1990; Guidotti and Dyar 1991), kimberlites and associated ultramafic xenoliths (Farmer and Boettcher 1981; Neal and Taylor 1989), and manganophillites (Jakob 1925). In particular, the above authors hypothesized the presence of Fe³⁺ in tetrahedral sites on the basis of optical observations (i.e., reverse pleochroism) and spectroscopic studies.

The study of the crystal structure of trioctahedral micas with Fe³⁺ tetrahedral content has thus far involved only (1) an Fe-rich phlogopite with composition (K_{0.9}Mn_{0.1})Mg₃-

[Si₃(Fe³⁺Mn)]O₁₀(OH)₂ (Steinfink 1962), for which significant Mn content in the interlayer sites was assumed; (2) a synthetic iron mica (ferriannite) with composition KFe₃⁺(Fe³⁺Si₃)O₁₀(OH)₂ (Donnay et al. 1964); (3) a ferriphlogopite and a ferribiotite (Semenova et al. 1977, 1983); (4) an alkali-rich trioctahedral mica (Hazen et al. 1981); and (5) phlogopite from mantle-derived rocks (Cruciani and Zanazzi 1992).

The Fe content of micas was recently identified using spectroscopic methods (i.e., Raman, infrared, and Mössbauer spectroscopies). In particular, Fe distribution between tetrahedral and octahedral sites was quantified by Dyar (1990) and Rancourt et al. (1992) using Mössbauer spectroscopy. These authors found that Fe³⁺ can be assigned to tetrahedral sites, whereas both Fe²⁺ and Fe³⁺ can be placed in octahedral sites. The presence of Fe³⁺ in tetrahedral sites was also confirmed by XANES investigation (Cruciani and Quartieri 1992). Partitioning of Fe³⁺ between tetrahedral and octahedral sites in phlogopite is

closely related to the physical-chemical conditions of crystallization, particularly f_{O_2} and Ti-Al contents.

This research deals with the crystal chemistry of phlogopite and Fe³⁺-rich phlogopite occurring in the Tapira alkaline-carbonatite complex, which outcrops about 300 km west of the city of Belo Horizonte, in the state of Minas Gerais, Brazil. The aim of this paper is to define the crystal-chemical characteristics of phlogopite and ferriphlogopite in order to assess their petrological significance and genetic condition. Because phlogopite crystals in the Tapira complex are found throughout the whole range of rocks (from dunite to carbonatite), their structural and compositional variations can be used to delineate the evolution of physical-chemical conditions in the magma chamber during differentiation and fractional crystallization processes. Their remarkably high Fe³⁺ content and low deformation make it possible to obtain satisfactory structural refinements.

PETROGRAPHY AND OCCURRENCE OF PHLOGOPITE

The Tapira complex belongs to a small group of layered alkaline-carbonatite intrusions (including Araxá and Salitre) located on the northeastern border of the Paraná Basin. These complexes are similar in age, ranging from 87 to 70 Ma (Herz 1977), and show analogous petrologic features. The Tapira complex has been dated as uppermost Cretaceous (69.5 ± 3.5 Ma) by use of the K-Ar method on biotite (Hasui and Cordani 1968) and consists of a subcircular plutonic body extending over an area of about 33 km² within the Precambrian basement of the Canastra Group (Ulbrich and Gomes 1981). This layered intrusion is composed mainly of alkaline-silicate and silicate-carbonatite rocks and very subordinate carbonatite. The complex has so far received attention for its Nb, P, and Ti deposits (Beurlen and Cassadane 1981), whereas its petrogenetic history is little known. The distribution of rock types as well as their field relationships are poorly known because of a thick lateritic cover (30–200 m). Consequently, all available geologic and petrologic data on the Tapira complex have been obtained by drillings scattered throughout the complex. The drilling data indicate that the layered intrusion is characterized by a cumulitic series with layers ranging from a few millimeters to several centimeters in thickness.

Because of the unusual mineralogic and chemical composition characterizing these rocks, the classification system adopted is mainly based on the petrographic study according to the nomenclature proposed by Johannsen (1951).

The alkaline-silicate rocks consist of dunite, wehrlite, clinopyroxenite (jacupirangite), and bebedourite; the silicate-carbonatite consist of garnet-magnetite, perovskite-magnetite, and glimmerite. The main intrusive body is crosscut by dykes and veins of variable thickness and composition (melilitite, lamprophyre, trachyte, and silexite). Dykes and veins represent about 15% of the

complex. Cumulus phases in dunite are represented by olivine and, occasionally, clinopyroxene (<5%), whereas the intercumulus phases consist mainly of apatite, phlogopite, calcite, ilmenite, variable amounts of perovskite, and, occasionally, titaniferous magnetite; schorlomite garnet and sulfides are accessory phases. Wehrlite paragenesis is very similar to that of dunite, except for the amount of subhedral clinopyroxene. Clinopyroxenite, with granular texture, consists of subhedral to euhedral green clinopyroxene and perovskite plus small amounts of euhedral apatite, anhedral phlogopite, calcite, ilmenite, and rare titaniferous magnetite. Bebedourite and glimmerite are the predominant rocks in the Tapira complex; they are mainly composed of Fe³⁺-rich phlogopite (30–50%), variable amounts of clinopyroxene (>20% in bebedourite and 0–20% in glimmerite), and subordinate perovskite, apatite, calcite, ilmenite, and titaniferous magnetite. Perovskite-bearing magnetite is composed of perovskite and occasional schorlomite garnet as primary cumulus phases, and magnetite and Fe³⁺-rich phlogopite as intercumulus phases. The crystallization order deduced from the cumulate rocks is olivine < apatite \pm clinopyroxene < perovskite < phlogopite < Fe³⁺-rich phlogopite \pm magnetite < carbonates. Consequently, the sequence of cumulitic rocks represented in the complex is as follows: dunite, wehrlite, clinopyroxenite, bebedourite, garnet-magnetite, perovskite-magnetite, glimmerite, and carbonatite.

In the ultramafic rocks of Tapira, magmatic phlogopite occurs as a subordinate phase in dunite, wehrlite, and clinopyroxenite, whereas it is a major component in bebedourite and glimmerite. Phlogopite originating from fenitization processes, which are recognizable on the basis of different optical characteristics, are only sporadically found and have not been investigated in this paper.

The major element composition of selected phlogopite-bearing rocks is reported in Table 1. The chemical composition of Tapira complex ultramafic rocks is clearly related to the cumulate nature of these rocks. The presence of variable amounts of nonsilicate phases is reflected by the generally low SiO₂ content (up to 44.22 wt%). TiO₂, although showing a wide range of variation, is usually abundant (1.51–46.16 wt%) and depends mainly on the amount of perovskite and titaniferous magnetite in the cumulus. All rock types display very low Al₂O₃ content (0–7.72 wt%); nevertheless, a progressive increase in Al₂O₃ from dunite to bebedourite, followed by a sharp decrease in perovskite-magnetite and glimmerite, is observed.

Like the alkaline-carbonatite complex of Juquiá, Brazil (Beccaluva et al. 1992), also composed of a subcircular, ultramafic cumulitic body with a carbonatitic core, the petrogenesis of the Tapira complex may be interpreted as the result of fractional crystallization and cumulus mechanisms from an alkaline-silicate parental magma, accompanied by silicate-carbonatite liquid immiscibility processes. Accordingly, the phlogopite samples studied in this paper can be referred to both as alkaline-silicate and silicate-carbonatite magmatic systems.

TABLE 1. Selected bulk-rock major element compositions for Tapira complex ultramafic rocks

| | Dunite* | Bebedourite | | | | Perovskite-magnetite | | | Glimmerite | |
|--------------------------------|----------|-------------|---------|----------|---------|----------------------|----------|---------|------------|----------|
| | Tas27-2B | Tag15-4 | Tag15-3 | Tpg63-2B | Tae23-1 | Tpq16-4A | Tpq16-4B | Tpt17-1 | Tas22-1 | Tpq16-6B |
| | wt% | | | | | | | | | |
| SiO ₂ | 10.91 | 24.06 | 23.85 | 29.51 | 44.22 | 20.68 | 1.06 | 1.41 | 25.22 | 16.82 |
| TiO ₂ | 11.52 | 7.33 | 8.35 | 4.02 | 1.51 | 7.63 | 46.16 | 25.86 | 5.78 | 3.49 |
| Al ₂ O ₃ | 1.66 | 3.08 | 3.56 | 3.42 | 7.72 | 1.07 | 0.21 | 0.55 | 0.00 | 0.00 |
| Fe ₂ O ₃ | 11.86 | 11.28 | 11.67 | 5.53 | 4.71 | 12.06 | 12.81 | 31.21 | 17.89 | 9.46 |
| FeO | 9.14 | 3.61 | 3.94 | 6.28 | 7.17 | 9.67 | 7.40 | 17.89 | 9.02 | 4.01 |
| MnO | 0.20 | 0.19 | 0.18 | 0.23 | 0.24 | 0.22 | 0.17 | 0.37 | 0.31 | 0.00 |
| MgO | 15.37 | 10.14 | 10.21 | 14.57 | 10.64 | 13.88 | 1.36 | 5.15 | 20.65 | 13.92 |
| CaO | 22.90 | 25.89 | 24.49 | 18.29 | 16.75 | 16.75 | 28.38 | 14.03 | 8.09 | 24.36 |
| Na ₂ O | 0.09 | 0.26 | 0.32 | 0.86 | 0.73 | 0.42 | 0.23 | 0.15 | 0.09 | 0.71 |
| K ₂ O | 1.12 | 2.04 | 2.39 | 3.58 | 2.82 | 4.18 | 0.25 | 0.20 | 5.14 | 3.04 |
| P ₂ O ₅ | 13.68 | 9.28 | 7.29 | 3.42 | 0.76 | 0.91 | 0.14 | 0.76 | 1.87 | 6.73 |
| H ₂ O ⁺ | 1.54 | 2.84 | 3.76 | 1.58 | 2.73 | 2.41 | 1.82 | 2.42 | 1.09 | 3.18 |
| CO ₂ | 0.00 | 0.00 | 0.00 | 8.69 | 0.00 | 10.11 | 0.00 | 0.00 | 4.84 | 14.28 |
| Sum | 100.00 | 100.00 | 100.00 | 100.00 | 100.00 | 100.00 | 100.00 | 100.00 | 100.00 | 100.00 |

Note: Key to sample labels is as follows: (1) The first two letters indicate a mining sector within the Tapira complex; (2) the third letter coupled with the first number indicates the exact location of drilling within the mining sector; (3) the number following the hyphen refers to the stratigraphic position in the drill core from bottom to top; and (4) a letter following the drill-core position number designates a single layer in compositionally layered samples.

* Apatite-bearing dunite.

ANALYTICAL METHODS

Major element analyses

Bulk-rock major element analyses (Table 1) were performed on powder pellets by X-ray fluorescence (XRF) using a PHILIPS PW 1400 spectrometer and following the matrix-correction method proposed by Franzini et al. (1975) and Leoni and Saitta (1976). Ferrous iron (FeO) was determined by titration method, H₂O by thermogravimetric analysis, and carbon dioxide (CO₂) by simple volumetric technique (calibrated using standard amounts of reagent grade CaCO₃ and checked by analyzing 20 reference samples with different CO₂ contents; mean relative percentage error of 3.8%; Jackson 1958).

Chemical analyses of phlogopite were conducted on both polished thin sections (Table 2) and on the crystals used for structure refinement (Table 3) by an ARL-SEMQ wavelength-dispersive electron microprobe. Ti and Ba contents were corrected for the overlap of the TiK and BaL peaks. F determination was obtained following the indications of Foley (1989); Cl was below the detection limit.

For crystals used in structure refinements, analyses of up to six points of the same crystal showed chemical homogeneity and were therefore averaged. Analyses of (OH)⁻ and Fe²⁺ were performed on a set of crystals from the samples used for structure refinement; H₂O weight percent was determined by thermogravimetric analysis in argon gas to minimize the reaction 2FeO + 2(OH)⁻ → Fe₂O₃ + H₂ + O²⁻, using a Seiko SSC5200 thermal analyzer (heating rate of 10 °C/min, flow rate of 200 mL/min). The determination was based on the weight loss observed in the temperature range 750–1200 °C and adjusted according to the F amount determined by microprobe analysis. The Fe²⁺ amount (estimated $\sigma < 4\%$) was determined by a semi-microvolumetric method (Meyrowitz 1970). For all samples, consistency and accuracy

of the Fe²⁺/Fe³⁺ ratio and (OH)⁻ content, experimentally obtained, were verified by a best-fit calculation involving structural parameters of well-refined phlogopite structures, both from this study and from the literature (Cruciani and Zanazzi 1994). Table 3 reports the oxide percentages and structural formulas based on O_{12-x-y-z}OH_xF_y.

For crystals analyzed on polished thin section (Table 2), the iterative method proposed by Dymek (1983) was used for the structural normalization procedure based on 11 O atoms [O₁₀(OH)₂] and evaluation of the FeO/(FeO + Fe₂O₃) ratio. Unfortunately, this method requires some assumptions that can affect the FeO/(FeO + Fe₂O₃) evaluation, especially when high-charge cations occupy the octahedral sites. In fact, the iterative calculation procedure assumes that Fe³⁺ fills the tetrahedra when the sum of ^[6](Si + Al) is <4 atoms per formula unit (apfu), whereas Ti and Fe³⁺ are located in octahedral sites according to the exchange vectors ^[6]Ti^[6]□^[6]Mg₋₂ and ^[6]Fe₂^[6]□^[6]Mg₋₃. Table 2 reports selected oxide percentages resulting from chemical analyses, as well as the apfu.

Single-crystal X-ray diffraction and structure refinement

Phlogopite crystals selected from crushed samples were first examined by Weissenberg and precession photographs. Crystals with sharp reflections and minimal streaking of $k \neq 3n$ were selected to determine cell dimensions and intensity data. The absence of $h + k \neq 2n$ reflections confirmed the C-centered unit cell. Following Bailey (1988), the intensity distribution along rows [13 l] and [02 l] was examined to determine the polytypic sequence. At least one crystal belonging to 1M polytype (mean space group C2/m) for each rock sample was selected for further investigation (different crystals from the same sample are labeled a, b, and c in the text and in

TABLE 2. Selected chemical data for Tapira complex phlogopite and ferriphlogopite samples

| | Dunite | Bebedourite | | | | Perovskite-magnetitite | | | | Glimmerite | |
|----------------------------------|--|-------------|---------|----------|---------|------------------------|-----------|------------|---------|------------|----------|
| | Tas27-2B | Tag15-4 | Tag15-3 | Tpg63-2B | Tae23-1 | Tpq16-4Aa | Tpq16-4Ab | Tpq16-4Ab' | Tpt17-1 | Tas22-1 | Tpq16-6B |
| | wt% | | | | | | | | | | |
| SiO ₂ | 39.49 | 37.00 | 36.54 | 35.67 | 39.48 | 40.49 | 40.36 | 40.11 | 39.41 | 40.71 | 40.49 |
| TiO ₂ | 1.04 | 1.93 | 2.39 | 3.13 | 1.55 | 0.53 | 0.46 | 0.51 | 1.48 | 0.20 | 0.21 |
| Al ₂ O ₃ | 12.74 | 14.22 | 13.62 | 13.40 | 12.33 | 8.86 | 7.71 | 5.66 | 12.69 | 0.00 | 0.38 |
| Fe ₂ O ₃ * | 4.89 | 9.25 | 9.81 | 13.34 | 5.21 | 9.11 | 10.85 | 13.16 | 4.22 | 20.48 | 21.70 |
| FeO | 1.10 | 2.60 | 2.58 | 3.03 | 1.49 | 0.61 | 0.60 | 0.56 | 1.34 | 0.00 | 0.36 |
| MgO | 25.09 | 20.25 | 19.73 | 16.75 | 24.79 | 25.14 | 24.82 | 24.99 | 25.24 | 24.44 | 23.29 |
| MnO | 0.02 | 0.15 | 0.17 | 0.33 | 0.07 | 0.11 | 0.16 | 0.13 | 0.05 | 0.10 | 0.15 |
| BaO | 0.58 | 1.01 | 1.07 | 0.61 | 0.70 | 0.06 | 0.09 | 0.04 | 0.61 | 0.05 | 0.02 |
| Na ₂ O | 0.29 | 0.15 | 0.22 | 0.09 | 0.34 | 0.10 | 0.10 | 0.10 | 0.06 | 0.13 | 0.12 |
| K ₂ O | 10.76 | 10.04 | 9.90 | 10.14 | 10.15 | 10.86 | 10.69 | 10.57 | 10.84 | 10.15 | 9.75 |
| F | 0.19 | 0.00 | 0.07 | 0.06 | 0.10 | 0.32 | 0.36 | 0.37 | 0.45 | 0.20 | 0.42 |
| Sum | 96.19 | 96.60 | 96.10 | 96.55 | 96.21 | 96.19 | 96.20 | 96.20 | 96.39 | 96.46 | 96.89 |
| Mg(%) | 97.6 | 93.3 | 93.2 | 90.8 | 96.7 | 98.7 | 98.7 | 98.8 | 97.1 | 100 | 99.1 |
| | Unit-cell content recalculated on the basis of O ₁₀ (OH) ₂ | | | | | | | | | | |
| Si | 2.82 | 2.68 | 2.67 | 2.63 | 2.81 | 2.92 | 2.92 | 2.93 | 2.81 | 3.03 | 3.01 |
| Al | 1.07 | 1.21 | 1.17 | 1.16 | 1.04 | 0.75 | 0.66 | 0.49 | 1.07 | 0.00 | 0.03 |
| Fe ³⁺ | 0.11 | 0.11 | 0.16 | 0.21 | 0.15 | 0.33 | 0.42 | 0.58 | 0.12 | 0.97 | 0.96 |
| Sum | 4.00 | 4.00 | 4.00 | 4.00 | 4.00 | 4.00 | 4.00 | 4.00 | 4.00 | 4.00 | 4.00 |
| Ti | 0.06 | 0.10 | 0.13 | 0.17 | 0.08 | 0.03 | 0.02 | 0.03 | 0.08 | 0.01 | 0.01 |
| Fe ³⁺ | 0.15 | 0.40 | 0.38 | 0.53 | 0.13 | 0.16 | 0.17 | 0.14 | 0.10 | 0.17 | 0.26 |
| Fe ²⁺ | 0.07 | 0.16 | 0.16 | 0.19 | 0.09 | 0.04 | 0.04 | 0.03 | 0.08 | 0.00 | 0.02 |
| Mg | 2.67 | 2.18 | 2.15 | 1.84 | 2.63 | 2.70 | 2.68 | 2.72 | 2.68 | 2.71 | 2.58 |
| Mn | 0.00 | 0.01 | 0.01 | 0.02 | 0.00 | 0.01 | 0.01 | 0.01 | 0.00 | 0.01 | 0.01 |
| Sum | 2.95 | 2.85 | 2.83 | 2.75 | 2.93 | 2.94 | 2.92 | 2.93 | 2.94 | 2.90 | 2.88 |
| Na | 0.04 | 0.02 | 0.03 | 0.01 | 0.05 | 0.01 | 0.01 | 0.01 | 0.01 | 0.02 | 0.02 |
| K | 0.98 | 0.93 | 0.92 | 0.95 | 0.92 | 1.00 | 0.99 | 0.99 | 0.98 | 0.96 | 0.93 |
| Ba | 0.01 | 0.03 | 0.03 | 0.02 | 0.02 | 0.00 | 0.00 | 0.00 | 0.02 | 0.00 | 0.00 |
| Sum | 1.03 | 0.98 | 0.98 | 0.98 | 0.99 | 1.01 | 1.00 | 1.00 | 1.01 | 0.98 | 0.95 |

Note: Labels a and b refer to different phlogopite crystals representative of different populations. Prime symbol in sample labeled Tpq16-4Ab refers to rim composition. The unit-cell content was recalculated according to Dymek (1983).

* Fe²⁺/Fe³⁺ was estimated according to the procedure of Dymek (1983).

Tables 3–9).¹ Furthermore, in all rock samples, 1M and disordered 1M stacking mostly coexist with twinned sequences.

Selected crystals [Tas27-2Ba, Tag15-4, Tag15-3, Tpg63-2B, Tae23-1(a–c), Tpq16-4A, Tas22-1(a, b), and Tpq16-6B] were mounted on an automated CAD4 (Enraf-Nonius) single-crystal X-ray diffractometer (MoK α graphite monochromatized radiation, at 52 kV and 40 mA operating conditions). Cell dimensions were determined using the 2 θ values for 25 centered reflections with 10° ≤ θ ≤ 25° (Table 4). Intensities were collected in the θ range 1.5–35° (–1 ≤ h ≤ 8, –14 ≤ k ≤ 14, –16 ≤ l ≤ 16) using the ω scan mode (scan rate of 1°/min, scan window of 3–5°, background time of 20 s). The unit-cell parameters and intensity data for crystals Tas27-2Bb and Tpt17-1 were obtained using a Siemens automated four-circle X-ray diffractometer with rotating anode (MoK α graphite monochromatized radiation, operating at 52 kV and 140 mA) and Siemens X-SCANS software. Cell parameters were determined using least-squares refinement of 60 medium-high angle reflections. Intensities were collected in the θ range 1.5–35° (–1 ≤ h ≤ 8, –14 ≤ k ≤ 14,

–16 ≤ l ≤ 16), using the ω scan mode (window width of 2.4 and 3° for phlogopite crystals Tas27-2Bb and Tpt17-1, respectively). For all crystals, Lorentz polarization corrections were made and adsorption effects were corrected using a complete scan (0–360° at 10° intervals in ψ) with more than five selected reflections. Intensity data of symmetrically equivalent reflections were averaged, the resulting discrepancy factor (R_{sym}) being in the range 0.015 ≤ R_{sym} ≤ 0.028 (Table 4).

Structure refinements were made by a full-matrix least-squares procedure, selecting reflections with $I \geq 5\sigma$, and using the ORFLS program (Busing et al. 1962). The atomic parameters reported by Brigatti and Davoli (1990) for the space group $C2/m$ were used as the initial values in each refinement. Fully ionized scattering factors were used for the nontetrahedral cations, whereas both neutral and ionized scattering factors were used for tetrahedral and anion sites (Brigatti and Davoli 1990). The initial scattering factors were Fe²⁺ vs. Mg²⁺ for M1 and M2 sites, K⁺ for the interlayer site, O vs. O²⁻ for anion sites, and a composite of 75% Si–25% Al vs. 75% Si⁴⁺–25% Al³⁺ for tetrahedral sites, whereas for samples Tas22-1(a, b) and Tpq16-6B a composite of 80% Si–20% Fe vs. 80% Si⁴⁺–20% Fe³⁺ was used. In the final part of anisotropic refinement, scattering curves adequate to the composition were applied, and at the final stage a difference-Fourier (ΔF) synthesis was calculated to locate H positions. The standard deviation of the ΔF peak (using the equation of Lipson and Cochran

¹ A copy of Tables 5, 7, and 9 may be ordered as Document AM-96-619 from the Business Office, Mineralogical Society of America, 1015 Eighteenth Street NW, Suite 601, Washington, DC 20036, U.S.A. Please remit \$5.00 in advance for the microfiche.

TABLE 3. Chemical data and mean atomic number of octahedral (M) and interlayer (K) sites for crystals used in the structure refinement

| | Dunite | | Bebedourite | | | Perovskite-magnetite | | | Glimmerite | | | | |
|--------------------------------|---|------------|-------------|----------|-----------|----------------------|-----------|-----------|------------|----------|-----------|-----------|-----------|
| | Tas 27-2Ba | Tas 27-2Bb | Tag 15-4 | Tag 15-3 | Tpg 63-2B | Tae 23-1a | Tae 23-1b | Tae 23-1c | Tpq 16-4A | Tpt 17-1 | Tas 22-1a | Tas 22-1b | Tpq 16-6B |
| | wt% | | | | | | | | | | | | |
| SiO ₂ | 39.82 | 39.91 | 37.30 | 37.41 | 36.00 | 39.51 | 39.57 | 39.41 | 39.76 | 39.24 | 41.47 | 40.84 | 41.71 |
| TiO ₂ | 1.02 | 1.02 | 2.30 | 2.38 | 3.16 | 1.55 | 1.69 | 1.89 | 0.52 | 1.49 | 0.23 | 0.20 | 0.31 |
| Al ₂ O ₃ | 12.76 | 13.01 | 13.66 | 13.33 | 13.52 | 12.33 | 13.39 | 13.57 | 8.21 | 13.05 | 0.00 | 0.00 | 0.51 |
| Fe ₂ O ₃ | 4.89 | 4.84 | 6.11 | 6.35 | 5.86 | 5.19 | 4.95 | 5.14 | 8.65 | 4.08 | 16.70 | 17.50 | 18.21 |
| FeO | 1.10 | 1.10 | 6.10 | 5.50 | 9.90 | 1.50 | 1.50 | 1.50 | 3.60 | 1.41 | 2.74 | 2.74 | 3.10 |
| MgO | 25.10 | 24.79 | 19.65 | 20.01 | 16.90 | 24.80 | 24.48 | 24.14 | 24.27 | 25.00 | 24.17 | 24.52 | 22.55 |
| MnO | 0.02 | 0.09 | 0.18 | 0.13 | 0.33 | 0.07 | 0.06 | 0.04 | 0.11 | 0.09 | 0.06 | 0.10 | 0.08 |
| BaO | 0.58 | 0.46 | 1.30 | 0.95 | 0.57 | 0.70 | 0.47 | 0.64 | 0.07 | 0.74 | 0.07 | 0.05 | 0.00 |
| Na ₂ O | 0.20 | 0.22 | 0.00 | 0.00 | 0.00 | 0.34 | 0.36 | 0.34 | 0.00 | 0.08 | 0.05 | 0.13 | 0.13 |
| K ₂ O | 10.57 | 10.51 | 9.76 | 9.81 | 10.23 | 10.16 | 9.67 | 9.52 | 10.64 | 10.75 | 10.37 | 10.19 | 9.86 |
| H ₂ O | 3.80 | 3.80 | 3.40 | 3.90 | 3.45 | 3.80 | 3.80 | 3.80 | 3.80 | 3.60 | 3.55 | 3.55 | 3.10 |
| F | 0.14 | 0.25 | 0.24 | 0.22 | 0.07 | 0.03 | 0.04 | 0.04 | 0.36 | 0.48 | 0.61 | 0.20 | 0.43 |
| Sum | 100.00 | 100.00 | 100.00 | 99.99 | 99.99 | 99.98 | 99.98 | 100.03 | 99.99 | 100.01 | 100.02 | 100.02 | 99.99 |
| | Unit-cell content recalculated on the basis of O _{12-x-y} (OH) _x F _y | | | | | | | | | | | | |
| Si | 2.85 | 2.85 | 2.76 | 2.74 | 2.71 | 2.84 | 2.82 | 2.81 | 2.91 | 2.82 | 3.11 | 3.07 | 3.15 |
| Al | 1.07 | 1.10 | 1.19 | 1.15 | 1.20 | 1.04 | 1.13 | 1.14 | 0.71 | 1.11 | 0.00 | 0.00 | 0.04 |
| Fe ³⁺ | 0.08 | 0.05 | 0.05 | 0.11 | 0.09 | 0.12 | 0.05 | 0.05 | 0.38 | 0.07 | 0.89 | 0.93 | 0.81 |
| Sum | 4.00 | 4.00 | 4.00 | 4.00 | 4.00 | 4.00 | 4.00 | 4.00 | 4.00 | 4.00 | 4.00 | 4.00 | 4.00 |
| Ti | 0.05 | 0.06 | 0.13 | 0.13 | 0.18 | 0.08 | 0.09 | 0.10 | 0.03 | 0.08 | 0.01 | 0.01 | 0.02 |
| Fe ³⁺ | 0.19 | 0.21 | 0.30 | 0.25 | 0.24 | 0.16 | 0.22 | 0.23 | 0.10 | 0.15 | 0.05 | 0.06 | 0.23 |
| Fe ²⁺ | 0.07 | 0.07 | 0.38 | 0.34 | 0.62 | 0.09 | 0.09 | 0.09 | 0.22 | 0.08 | 0.17 | 0.17 | 0.20 |
| Mg | 2.68 | 2.64 | 2.17 | 2.19 | 1.90 | 2.65 | 2.60 | 2.57 | 2.64 | 2.68 | 2.70 | 2.75 | 2.54 |
| Mn | 0.00 | 0.01 | 0.01 | 0.01 | 0.02 | 0.00 | 0.00 | 0.00 | 0.01 | 0.01 | 0.00 | 0.01 | 0.00 |
| Sum | 2.99 | 2.99 | 2.99 | 2.92 | 2.96 | 2.98 | 3.00 | 2.99 | 3.00 | 3.00 | 2.93 | 3.00 | 2.99 |
| Na | 0.03 | 0.03 | 0.00 | 0.00 | 0.00 | 0.05 | 0.05 | 0.05 | 0.00 | 0.01 | 0.01 | 0.02 | 0.02 |
| K | 0.96 | 0.96 | 0.92 | 0.92 | 0.98 | 0.93 | 0.88 | 0.87 | 0.99 | 0.98 | 0.99 | 0.98 | 0.95 |
| Ba | 0.01 | 0.01 | 0.04 | 0.02 | 0.02 | 0.02 | 0.01 | 0.02 | 0.00 | 0.02 | 0.00 | 0.00 | 0.00 |
| Sum | 1.00 | 1.00 | 0.96 | 0.94 | 1.00 | 1.00 | 0.94 | 0.94 | 0.99 | 1.01 | 1.00 | 1.00 | 0.97 |
| OH | 1.81 | 1.81 | 1.68 | 1.91 | 1.73 | 1.82 | 1.81 | 1.81 | 1.86 | 1.73 | 1.78 | 1.78 | 1.56 |
| F | 0.03 | 0.06 | 0.06 | 0.05 | 0.02 | 0.01 | 0.01 | 0.01 | 0.08 | 0.11 | 0.14 | 0.05 | 0.10 |
| O | 10.16 | 10.13 | 10.26 | 10.04 | 10.25 | 10.17 | 10.18 | 10.18 | 10.06 | 10.16 | 10.08 | 10.17 | 10.34 |
| Sum | 12.00 | 12.00 | 12.00 | 12.00 | 12.00 | 12.00 | 12.00 | 12.00 | 12.00 | 12.00 | 12.00 | 12.00 | 12.00 |
| | Mean atomic number (e ⁻) | | | | | | | | | | | | |
| M1 Xref | 14.0(1) | 13.7(1) | 15.7(1) | 14.9(1) | 16.8(1) | 13.4(1) | 13.5(1) | 14.0(1) | 13.8(1) | 13.8(1) | 12.9(1) | 13.9(1) | 14.6(1) |
| M2 Xref | 13.1(1) | 13.3(1) | 15.6(1) | 14.8(1) | 16.5(1) | 13.3(1) | 13.5(1) | 13.7(1) | 13.6(1) | 13.4(1) | 12.8(1) | 13.1(1) | 13.8(1) |
| M1 + M2 | | | | | | | | | | | | | |
| Xref* | 40.2 | 40.3 | 46.9 | 44.4 | 49.8 | 40.0 | 40.6 | 41.3 | 41.0 | 40.6 | 38.5 | 40.1 | 42.3 |
| M1 + M2 | | | | | | | | | | | | | |
| EPMA** | 40.0 | 40.5 | 46.8 | 44.7 | 49.6 | 40.1 | 41.2 | 41.4 | 40.9 | 40.2 | 38.3 | 39.4 | 42.1 |
| K Xref | 18.8(1) | 19.6(1) | 19.3(1) | 18.3(1) | 19.0(1) | 18.9(1) | 18.3(1) | 18.4(1) | 19.2(1) | 19.6(1) | 18.2(1) | 18.0(1) | 18.1(1) |
| K EPMA | 19.1 | 19.1 | 19.7 | 18.6 | 19.7 | 19.3 | 17.8 | 18.2 | 18.8 | 19.8 | 18.9 | 18.8 | 18.3 |

Note: Xref: X-ray refinement; EPMA: electron microprobe. Labels a, b, and c refer to different refined crystals coming from the same rock sample. Standard deviations are given in parentheses.

* 2M2 + M1.

** Sum of octahedral cation electrons.

TABLE 4. Selected crystal data and unit-cell parameters for Tapira phlogopite and ferriphlogopite

| Samples | Dimensions (mm) | N _{obs} | R _{sym} (×100) | R _{obs} (×100) | a (Å) | b (Å) | c (Å) | β (°) | V (Å ³) |
|-----------|--------------------|------------------|-------------------------|-------------------------|-----------|-----------|------------|-----------|---------------------|
| Tas27-2Ba | 0.18 × 0.16 × 0.03 | 622 | 1.5 | 2.8 | 5.318(2) | 9.214(1) | 10.279(2) | 100.01(2) | 496.0 |
| Tas27-2Bb | 0.18 × 0.17 × 0.03 | 900 | 1.9 | 2.5 | 5.330(1) | 9.2346(7) | 10.3010(7) | 99.92(1) | 499.4 |
| Tag15-4 | 0.21 × 0.18 × 0.03 | 477 | 2.0 | 2.8 | 5.333(1) | 9.238(2) | 10.267(2) | 99.96(2) | 498.2 |
| Tag15-3 | 0.30 × 0.24 × 0.02 | 293 | 2.0 | 2.8 | 5.329(2) | 9.228(2) | 10.258(3) | 100.03(3) | 496.7 |
| Tpg63-2B | 0.39 × 0.15 × 0.02 | 543 | 2.2 | 2.3 | 5.3405(8) | 9.244(2) | 10.253(3) | 100.09(2) | 498.3 |
| Tae23-1a | 0.33 × 0.21 × 0.03 | 575 | 2.0 | 2.7 | 5.321(1) | 9.211(2) | 10.287(1) | 99.93(1) | 496.6 |
| Tae23-1b | 0.36 × 0.20 × 0.05 | 757 | 2.2 | 2.7 | 5.330(2) | 9.230(3) | 10.256(4) | 99.92(3) | 497.0 |
| Tae23-1c | 0.32 × 0.18 × 0.03 | 597 | 2.1 | 3.0 | 5.318(1) | 9.219(3) | 10.274(4) | 99.88(3) | 496.2 |
| Tpq16-4A | 0.42 × 0.38 × 0.05 | 797 | 2.2 | 2.8 | 5.338(2) | 9.247(1) | 10.300(2) | 99.96(2) | 500.8 |
| Tpt17-1 | 0.17 × 0.15 × 0.03 | 826 | 2.6 | 2.8 | 5.332(1) | 9.239(2) | 10.291(2) | 99.94(2) | 499.3 |
| Tas22-1a | 0.30 × 0.30 × 0.02 | 419 | 2.8 | 3.2 | 5.357(2) | 9.270(4) | 10.319(4) | 99.96(3) | 504.7 |
| Tas22-1b | 0.21 × 0.18 × 0.09 | 699 | 1.9 | 3.3 | 5.358(2) | 9.277(3) | 10.308(2) | 99.99(4) | 504.6 |
| Tpq16-6B | 0.27 × 0.15 × 0.09 | 766 | 2.2 | 3.1 | 5.356(1) | 9.284(2) | 10.309(3) | 100.03(2) | 504.8 |

Note: R_{sym} = $\frac{\sum_{hk\ell} \sum_{h_1k_1\ell_1} |I_{hk\ell} - I_{h_1k_1\ell_1}|}{\sum_{hk\ell} \sum_{h_1k_1\ell_1} I_{hk\ell}}$. Labels a, b, and c refer to different refined crystals. Standard deviations are given in parentheses.

TABLE 6. Selected bond lengths (in angstroms)

| | Tas 27-2Ba | Tas 27-2Bb | Tag 15-4 | Tag 15-3 | Tpg 63-2B | Tae 23-1a | Tae 23-1b | Tae 23-1c | Tpq 16-4A | Tpt 17-1 | Tas 22-1a | Tas 22-1b | Tpq 16-6B |
|--------------------------------------|---------------|---------------|-------------|-------------|--------------|--------------|--------------|--------------|--------------|-------------|--------------|--------------|--------------|
| T-O1 | 1.659(1) | 1.664(1) | 1.657(2) | 1.657(2) | 1.656(1) | 1.662(1) | 1.661(1) | 1.656(2) | 1.662(1) | 1.666(1) | 1.672(2) | 1.676(2) | 1.676(1) |
| T-O2 | 1.662(2) | 1.662(1) | 1.660(2) | 1.657(4) | 1.660(2) | 1.663(2) | 1.661(2) | 1.653(2) | 1.663(2) | 1.666(2) | 1.654(4) | 1.676(3) | 1.670(2) |
| T-O2' | 1.658(2) | 1.664(1) | 1.660(3) | 1.663(3) | 1.660(2) | 1.659(2) | 1.661(2) | 1.662(2) | 1.664(2) | 1.664(2) | 1.686(4) | 1.678(3) | 1.678(2) |
| T-O3 | 1.646(2) | 1.652(1) | 1.665(2) | 1.654(4) | 1.660(2) | 1.651(2) | 1.648(2) | 1.663(2) | 1.659(2) | 1.654(1) | 1.668(3) | 1.676(2) | 1.668(2) |
| ⟨T-O⟩ | 1.656 | 1.660 | 1.661 | 1.658 | 1.659 | 1.659 | 1.658 | 1.659 | 1.662 | 1.662 | 1.670 | 1.676 | 1.673 |
| M1-O3 (×4) | 2.090(2) | 2.092(1) | 2.091(2) | 2.094(3) | 2.098(2) | 2.087(2) | 2.090(2) | 2.088(2) | 2.097(2) | 2.093(1) | 2.103(3) | 2.099(2) | 2.105(2) |
| M1-O4 (×2) | 2.053(3) | 2.058(2) | 2.064(3) | 2.066(4) | 2.066(2) | 2.057(3) | 2.058(2) | 2.053(3) | 2.058(2) | 2.058(2) | 2.059(4) | 2.064(3) | 2.064(2) |
| ⟨M1-O⟩ | 2.078 | 2.081 | 2.082 | 2.085 | 2.087 | 2.077 | 2.079 | 2.076 | 2.084 | 2.081 | 2.088 | 2.087 | 2.091 |
| M2-O3 (×2) | 2.082(2) | 2.084(1) | 2.087(3) | 2.086(4) | 2.093(2) | 2.080(2) | 2.082(2) | 2.075(2) | 2.086(2) | 2.086(2) | 2.084(3) | 2.091(2) | 2.096(2) |
| M2-O3' (×2) | 2.088(2) | 2.094(1) | 2.090(2) | 2.093(3) | 2.088(2) | 2.090(2) | 2.093(2) | 2.079(2) | 2.096(2) | 2.092(1) | 2.112(3) | 2.095(2) | 2.101(2) |
| M2-O4 (×2) | 2.060(2) | 2.066(1) | 2.056(2) | 2.056(4) | 2.056(2) | 2.062(2) | 2.060(2) | 2.064(2) | 2.065(2) | 2.061(1) | 2.070(3) | 2.070(2) | 2.070(2) |
| ⟨M2-O⟩ | 2.077 | 2.082 | 2.078 | 2.078 | 2.079 | 2.077 | 2.078 | 2.073 | 2.082 | 2.080 | 2.089 | 2.085 | 2.089 |
| K ⁺ -O1 (×2) | 3.365(3) | 3.372(2) | 3.372(4) | 3.360(6) | 3.364(3) | 3.380(3) | 3.380(3) | 3.384(3) | 3.395(3) | 3.381(2) | 3.456(6) | 3.441(4) | 3.421(3) |
| K ⁺ -O1' (×2) | 2.978(3) | 2.986(2) | 2.984(4) | 2.983(5) | 2.993(3) | 2.969(3) | 2.974(3) | 2.972(4) | 2.979(3) | 2.974(2) | 2.947(6) | 2.942(4) | 2.952(3) |
| K ⁺ -O2 (×4) | 3.363(2) | 3.372(2) | 3.371(3) | 3.368(3) | 3.357(2) | 3.374(2) | 3.380(2) | 3.375(3) | 3.393(2) | 3.378(2) | 3.441(4) | 3.440(3) | 3.423(2) |
| K ⁺ -O2' (×4) | 2.981(2) | 2.986(1) | 2.979(3) | 2.974(4) | 2.988(2) | 2.973(2) | 2.974(2) | 2.976(2) | 2.977(2) | 2.978(2) | 2.955(4) | 2.941(3) | 2.957(2) |
| ⟨K ⁺ -O⟩ _{inner} | 2.980 | 2.986 | 2.981 | 2.977 | 2.990 | 2.972 | 2.974 | 2.975 | 2.978 | 2.977 | 2.953 | 2.941 | 2.955 |
| ⟨K ⁺ -O⟩ _{outer} | 3.364 | 3.372 | 3.371 | 3.365 | 3.359 | 3.376 | 3.380 | 3.378 | 3.394 | 3.379 | 3.446 | 3.440 | 3.422 |
| Δ⟨K ⁺ -O⟩ | 0.384 | 0.386 | 0.390 | 0.388 | 0.369 | 0.404 | 0.406 | 0.403 | 0.416 | 0.402 | 0.493 | 0.499 | 0.467 |

Note: Labels a, b, and c as in Table 4. Standard deviations are given in parentheses.

* K indicates interlayer cation.

1953) ranged from 0.05 to 0.08 e/Å³. A careful examination of the final ΔF map for samples Tas27-2B(a, b), Tag15-3, Tae23-1(a, c), Tpq16-4A, and Tpt17-1 showed a peak above background (≥3σ) [indicating a reasonable O-H bond length (0.90–1.10 Å) located in proximity to the O4 atom], which can be attributed to the H⁺ position.

The peak heights are in the 0.6–0.9 e/Å³ range. Crystallographic coordinates and temperature parameters are listed in Table 5; relevant bond lengths are shown in Table 6, and the effective bond lengths calculated according to Downs et al. (1992) are reported in Table 7. Selected tetrahedral, octahedral, and interlayer parameters are re-

TABLE 8. Selected tetrahedral, octahedral, and interlayer parameters derived from structure refinement

| | Tas27-2Ba | Tas27-2Bb | Tag15-4 | Tag15-3 | Tpg63-2B | Tae23-1a |
|-----------------------------------|-----------|-----------|----------|----------|----------|----------|
| β _{ideal} (°) | 99.93 | 99.93 | 99.97 | 99.97 | 100.00 | 99.93 |
| Tetrahedral parameters | | | | | | |
| α (°) | 8.5 | 8.5 | 8.6 | 8.5 | 8.1 | 8.9 |
| Δz (Å) | 0.0007 | 0.0009 | 0.0053 | 0.0011 | 0.0089 | 0.0003 |
| τ (°) | 110.7(1) | 110.7(1) | 110.2(2) | 110.4(1) | 110.2(1) | 110.6(1) |
| TQE | 1.0004 | 1.0004 | 1.0002 | 1.0003 | 1.0002 | 1.0004 |
| TAV | 1.87 | 1.86 | 1.87 | 1.09 | 0.64 | 1.70 |
| V _r (Å ³) | 2.330 | 2.348 | 2.349 | 2.338 | 2.343 | 2.340 |
| ⟨O1-O2⟩ (Å) | 2.689 | 2.695 | 2.697 | 2.693 | 2.696 | 2.692 |
| Octahedral parameters | | | | | | |
| ψ _{M1} (°) | 58.63 | 58.62 | 58.82 | 58.69 | 58.84 | 58.64 |
| ψ _{M2} (°) | 58.61 | 58.64 | 58.75 | 58.59 | 58.71 | 58.64 |
| e _u /e _{m1} | 1.0986 | 1.0980 | 1.1031 | 1.0999 | 1.1040 | 1.0983 |
| e _u /e _{m2} | 1.0980 | 1.0984 | 1.1014 | 1.0972 | 1.1003 | 1.0986 |
| OQE _{M1} | 1.0097 | 1.0096 | 1.0106 | 1.0099 | 1.0108 | 1.0097 |
| OQE _{M2} | 1.0096 | 1.0097 | 1.0103 | 1.0095 | 1.0100 | 1.0098 |
| OAV _{M1} | 31.85 | 31.49 | 34.67 | 32.52 | 35.22 | 31.88 |
| OAV _{M2} | 31.83 | 32.17 | 33.74 | 31.20 | 33.07 | 32.27 |
| V _{M1} (Å ³) | 11.791 | 11.842 | 11.846 | 11.904 | 11.929 | 11.772 |
| V _{M2} (Å ³) | 11.770 | 11.856 | 11.779 | 11.805 | 11.807 | 11.772 |
| Sheet thickness (Å) | | | | | | |
| Tetrahedral | 2.256 | 2.262 | 2.258 | 2.251 | 2.252 | 2.258 |
| Octahedral | 2.613 | 2.167 | 2.156 | 2.167 | 2.160 | 2.162 |
| Interlayer separation | 3.447 | 3.455 | 3.441 | 3.433 | 3.431 | 3.455 |

Note: α (tetrahedral rotation angle) = Σ_{i=1}⁴ α_i/6, where α_i = |120° - φ_i|/2 and where φ_i is the angle between basal edges of neighboring tetrahedra articulated in the ring; Δz = [Z_{(O_{outer})max} - Z_{(O_{inner})min}]/[c sin β]; τ (tetrahedral flattening angle) = Σ_{i=1}⁴ [(O_{apical})_i-T-O_(base)]/3; TAV (tetrahedral angle variance) = Σ_{i=1}⁴ θ_i - 109.47°/5 (Robinson et al., 1971); TQE (tetrahedral quadratic elongation) = Σ_{i=1}⁴ (l_i/l₀)²/4, where l₀ is the center-to-vertex distance for an undistorted tetrahedron, the volume of which is equal to that of the distorted tetrahedron with bond length l_i (Robinson et al. 1971); ψ (octahedral flattening angle) = cos⁻¹ [octahedral thickness / (2 (M-O))] (Donnay et al. 1964); e_u, e_m = mean lengths of unshared and shared edges, respectively (Toraya 1981); OQE (octahedral quadratic elongation) = Σ_{i=1}⁶ (l_i/l₀)²/6, where l₀ is the center-to-vertex distance for an undistorted octahedron, the volume of which is equal to that of the distorted octahedron with bond length l_i (Robinson et al. 1971); OAV (octahedral angle variance) = Σ_{i=1}⁶ (θ_i - 90°)²/11 (Robinson et al. 1971). Labels a, b, and c as in Table 4. Standard deviations are given in parentheses.

ported in Table 8, and mean atomic numbers of cation sites, as estimated by structure refinement and electron probe microanalyses, are reported and compared in Table 3. Observed and calculated structure factors are reported in Table 9.

DISCUSSION

Textural and optical features of phlogopite

Magmatic phlogopite from the Tapira complex displays a wide range of textural and optical characteristics, which, in turn, closely reflect the conditions under which the various occurrences of phlogopite formed, as suggested by Farmer and Boettcher (1981) and Neal and Taylor (1989).

In dunite, wehrlite, and clinopyroxenite, phlogopite crystals are interstitial and display subhedral to anhedral forms. They generally show weak normal pleochroism, ranging from α = pale yellow to $\gamma \cong \beta$ = yellow. However, small amounts of crystals showing reverse pleochroism are also found; their occurrence increases gradually from dunite to clinopyroxenite. In bebedourite, phlogopite is characterized by more significant zoning, usually revealed by a core with normal pleochroism and a rim with more intense reverse pleochroism (α = reddish; $\gamma \cong \beta$ = orange-yellow). Although most phlogopite crystals have this type of zoning, others display oscillatory patterns. Moreover, unzoned, smaller crystals with compo-

sitions similar to that of the zoned crystal rims are also found. Subhedral to euhedral crystals of ferriphlogopite predominate in perovskite-magnetite and glimmerite; they show intense reverse pleochroism varying from α = red to $\gamma \cong \beta$ = orange. In glimmerite, hematitic rims of various thickness developing around phlogopite crystals are occasionally observed.

Phlogopite chemistry

Representative phlogopite compositions are reported in Tables 2 and 3. The number of apfu (listed in Table 2) was calculated using the normalization procedure proposed by Dymek (1983) for crystals analyzed on polished thin sections, whereas the chemical formulas shown in Table 3 are for crystals used in the structure refinement (see the Analytical Methods section for further details) and are based on $O_{12-x-y}OH_xF_y$.

The chemistry of Tapira phlogopite is characterized by high variability among different rock types (Fig. 1). In fact, phlogopite from glimmerite shows high Fe_{tot} , Mg, and Si contents ($1.0 \leq Fe_{tot} \leq 1.3$, $2.5 \leq Mg \leq 2.9$, $Si \cong 3.0$ apfu) and very low Al and Ti contents ($0.0 \leq Al \leq 0.1$ and $Ti \cong 0.0$ apfu); phlogopite from bebedourite shows marked differences in Fe_{tot} , Mg, and Ti contents ($0.3 \leq Fe_{tot} \leq 1.0$, $1.5 \leq Mg \leq 2.6$, $0.0 \leq Ti \leq 0.3$ apfu), whereas Al remains quite constant ($1.0 \leq Al \leq 1.3$ apfu). Phlogopite from dunite and perovskite-magnetite shows

TABLE 8.—Continued

| | Tae23-1b | Tae23-1c | Tpq16-4A | Tpt17-1 | Tas22-1a | Tas22-1b | Tpq16-6B |
|-------------------------------|----------|----------|----------|----------|----------|----------|----------|
| β_{obsd} (°) | 99.98 | 99.94 | 99.95 | 99.95 | 99.96 | 99.98 | 99.97 |
| Tetrahedral parameters | | | | | | | |
| α (°) | 8.9 | 8.9 | 9.1 | 8.8 | 10.8 | 10.9 | 10.2 |
| Δz (Å) | 0.0006 | 0.0067 | 0.0031 | 0.0007 | 0.0021 | 0.0007 | 0.0040 |
| τ (°) | 110.3(1) | 110.2(1) | 110.2(1) | 110.7(1) | 109.6(2) | 110.1(1) | 110.2(1) |
| TQE | 1.0002 | 1.0002 | 1.0001 | 1.0004 | 1.0001 | 1.0001 | 1.0001 |
| TAV | 0.92 | 0.80 | 0.64 | 1.76 | 0.26 | 0.43 | 0.62 |
| V_T (Å ³) | 2.338 | 2.341 | 2.356 | 2.356 | 2.390 | 2.418 | 2.401 |
| (O1-O2) (Å) | 2.698 | 2.693 | 2.704 | 2.699 | 2.724 | 2.727 | 2.722 |
| Octahedral parameters | | | | | | | |
| ψ_{M1} (°) | 58.74 | 58.83 | 58.71 | 58.75 | 58.72 | 58.91 | 58.77 |
| ψ_{M2} (°) | 58.73 | 58.76 | 58.69 | 58.72 | 58.74 | 58.87 | 58.73 |
| e_u/e_{M1} | 1.1012 | 1.1035 | 1.1007 | 1.1016 | 1.1008 | 1.1057 | 1.1019 |
| e_u/e_{M2} | 1.1009 | 1.1019 | 1.0999 | 1.1007 | 1.1011 | 1.1048 | 1.1011 |
| OQE _{M1} | 1.0102 | 1.0107 | 1.0101 | 1.0103 | 1.0101 | 1.0111 | 1.0104 |
| OQE _{M2} | 1.0102 | 1.0103 | 1.0100 | 1.0102 | 1.0104 | 1.0109 | 1.0102 |
| OAV _{M1} | 33.43 | 34.88 | 32.97 | 33.66 | 32.94 | 36.15 | 33.91 |
| OAV _{M2} | 33.65 | 34.06 | 33.03 | 33.58 | 33.88 | 35.77 | 33.67 |
| V_{M1} (Å ³) | 11.802 | 11.749 | 11.887 | 11.836 | 11.958 | 11.928 | 12.002 |
| V_{M2} (Å ³) | 11.791 | 11.690 | 11.864 | 11.810 | 11.966 | 11.897 | 11.968 |
| Sheet thickness (Å) | | | | | | | |
| Tetrahedral | 2.248 | 2.257 | 2.256 | 2.266 | 2.253 | 2.271 | 2.270 |
| Octahedral | 2.158 | 2.149 | 2.165 | 2.159 | 2.168 | 2.156 | 2.168 |
| Interlayer separation | 3.450 | 3.458 | 3.467 | 3.446 | 3.489 | 3.454 | 3.443 |

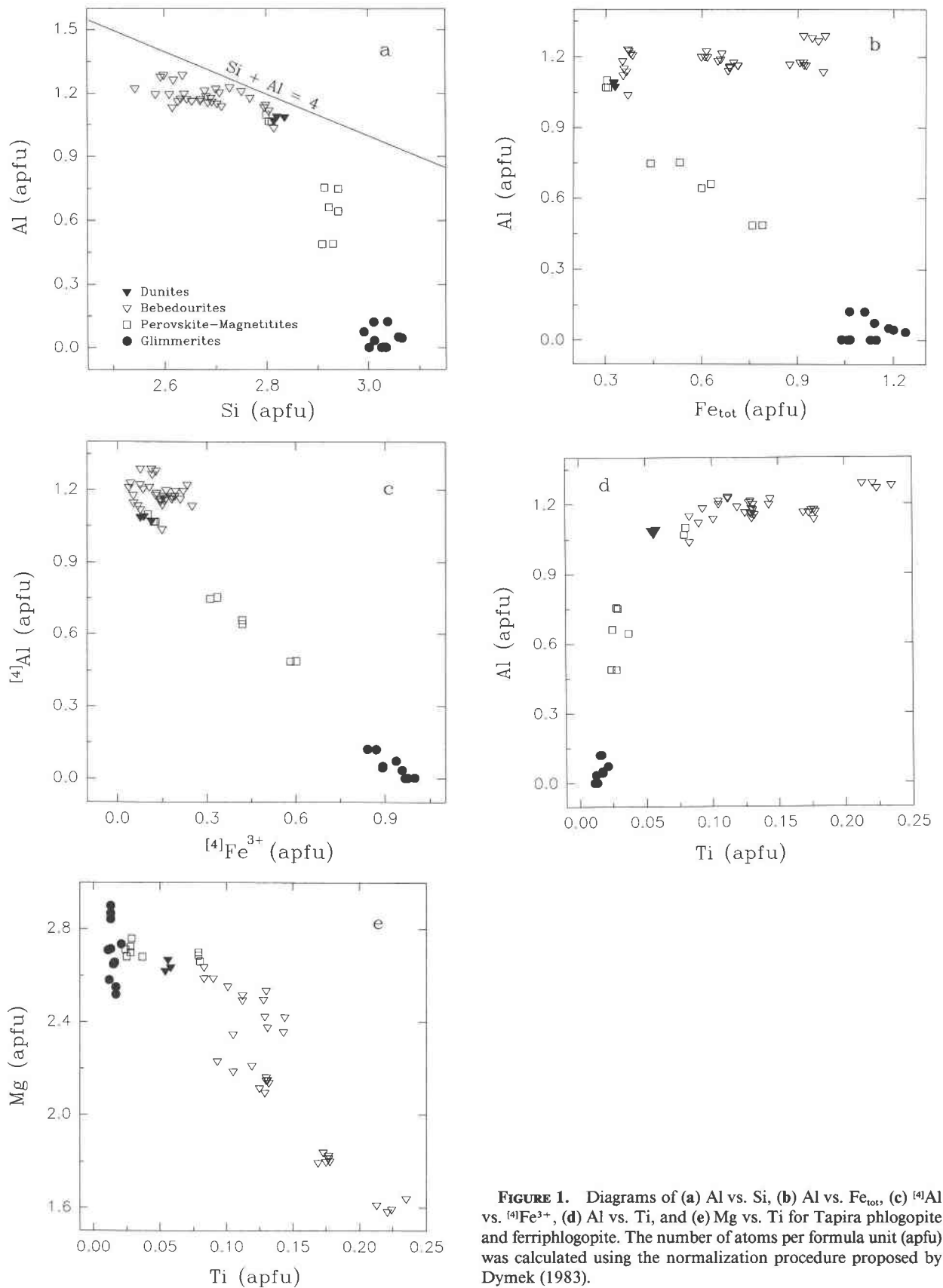


FIGURE 1. Diagrams of (a) Al vs. Si, (b) Al vs. Fe_{tot} , (c) $^{[4]}\text{Al}$ vs. $^{[4]}\text{Fe}^{3+}$, (d) Al vs. Ti, and (e) Mg vs. Ti for Tapira phlogopite and ferriphlogopite. The number of atoms per formula unit (apfu) was calculated using the normalization procedure proposed by Dymek (1983).

a chemical composition intermediate between glimmerite and bebedourite ($0.4 \leq \text{Al} \leq 1.1$, $0.3 \leq \text{Fe}_{\text{tot}} \leq 0.8$, $0.0 \leq \text{Ti} \leq 0.1$, $2.6 \leq \text{Mg} \leq 2.8$ apfu).

In all studied phlogopite samples, then, the Mg octahedral occupancy is in the range of $1.5 \leq {}^{60}\text{Mg} \leq 2.9$ apfu, whereas tetrahedral Si is substituted by Al, Fe³⁺, or both in the range $2.5 \leq {}^{44}\text{Si} \leq 3.1$ apfu. In tetrahedral sites, Al can be either partially or completely substituted by Fe³⁺. However, Figure 1a shows that Si and Al in tetrahedral sites is always <4 apfu. For this reason, the Tapira complex micas can be said to include phlogopite and ferriphlogopite (Bailey 1984).

Figure 1b shows that Fe_{tot} and Al contents are negatively correlated in the range 0.0–1.1 apfu Al (correlation coefficient $r = -0.978$) and that the analytical points plot close to the line Fe_{tot}/Al = 1. Above the Al value of 1.1 apfu, Fe_{tot} increases, whereas Al remains fairly constant. The ⁴⁴Al vs. ⁴⁴Fe³⁺ plot in Figure 1c indicates that the exchange vector ⁴⁴Fe³⁺+⁴⁴Al₋₁ is the main tetrahedral substitution in Tapira phlogopite crystals. Figure 1d shows the relationships between Al and Ti contents. In micas from perovskite magnetite and glimmerite, Ti remains constant, but Al strongly increases. In micas from dunite and bebedourite, in contrast, Al remains almost constant, but Ti sharply increases from 0.05 to 0.25 apfu. Furthermore, in dunite and bebedourite, phlogopite shows the lowest ⁴⁴Fe³⁺-for-⁴⁴Al substitution, and ⁶⁰Ti is negatively related to ⁶⁰Mg (Fig. 1e). The analytical data points do not fall exactly on the exchange vector ⁶⁰Ti⁶⁰□⁶⁰Mg₋₂, which suggests the presence of ⁴⁴Al₂⁶⁰Ti⁴⁴Si₋₂⁶⁰Mg₋₁ and ⁶⁰TiO₂⁶⁰Mg₋₁(OH)₋₂. In glimmerite and perovskite magnetite, the limited Mg substitution does not allow the identification of the presence of appreciable exchange vectors. In addition, we observed that, in samples showing the tetrahedral ⁴⁴Fe³⁺+⁴⁴Al₋₁ exchange vector, the Mg octahedral content seems to be higher, K is the main interlayer cation, and Ba-for-K substitutions are always below 4% of the site occupancy.

Crystal structure and crystal chemistry

In the next section, the structural data from Tapira phlogopite samples (Tables 6 and 8) are compared with data from crystals in the phlogopite-annite join reported in the literature (Joswig 1972; Hazen and Burnham 1973; Takeda and Ross 1975; Brigatti and Davoli 1990; Brigatti et al. 1991; Brigatti and Poppi 1993; Bigi and Brigatti 1994).

Tetrahedral sheet and interlayer sites. The tetrahedra are quite regular ($1.0001 \leq \text{TQE} \leq 1.0004$, $0.26 \leq \text{TAV} \leq 1.87$; TQE and TAV as defined by Robinson et al. 1971) and slightly elongated ($109.6^\circ \leq \tau \leq 110.7^\circ$; $\tau = 109.47^\circ$ for ideal tetrahedron, Table 8). Furthermore, tetrahedral mean bond lengths ($1.656 \text{ \AA} \leq \langle \text{T-O} \rangle \leq 1.676 \text{ \AA}$, Table 6) are greater than those normally observed for phlogopite, although the tetrahedral substitution, ranging between 21 and 33%, is in some cases below the ideal value of 25% (Table 3). As discussed by several authors (for a review, see Bailey 1984), the increase in tetrahedral

volume in trioctahedral micas can be modeled as a linear combination of ⁴⁴Al-for-⁴⁴Si substitution, which in turn produces an increase in basal edges and more flattened tetrahedra. In contrast, the tetrahedral enlargement in Tapira phlogopite can be negatively correlated with the tetrahedral substitution. This behavior implies the presence of a cation larger than Al, such as Fe (Fig. 2a). The tetrahedral volume increase, as a function of ⁴⁴Fe³⁺ substitution, is enhanced in samples Tas22-1(a, b) and Tpq16-6B, where Si content is >3.0 apfu and the tetrahedral volumes range between 2.39 and 2.42 Å³.

The tetrahedral basal-edge bond lengths (O1-O2) steadily increase as a function of ⁴⁴Fe³⁺ (Tables 3 and 8); the stretch trend is enhanced when ⁴⁴Fe³⁺ > 0.2 apfu. This increase in ⁴⁴Fe³⁺ content is accompanied by a significant reduction in shorter (K-O)_{inner} and an increase in longer (K-O) bond distances ((K-O)_{outer}); this leads to a greater difference Δ(K-O) and to an increase in distortion of the tetrahedral ring ($8.1^\circ \leq \alpha \leq 10.9^\circ$) (Figs. 2b and 2d). The above considerations are in agreement with the exchange vector ⁴⁴Fe³⁺+⁴⁴Al₋₁, although the Si content is greater than expected for a 1:1 substitution in Fe³⁺-rich crystals. In crystals with ⁴⁴Fe³⁺ ≤ 0.2 apfu, (K-O)_{inner} bond-distance variation cannot be related to tetrahedral features. As shown in Figure 2c, with the exception of phlogopite from dunite, (K-O)_{inner} bond distance depends on Ti content. This observation is related to the conclusions of Cruciani and Zanazzi (1994), who related the tetrahedral hole geometry to the loss of the proton at O4 resulting from the Ti-oxy substitution.

Similar to the Mg-rich micas studied by Takeda and Ross (1975), Ohta et al. (1982), and Cruciani and Zanazzi (1994), our crystals show high α values. This feature, in addition to the low F and Ba contents in the ditrigonal hole, is required to fit tetrahedral and octahedral sheet dimensions.

Table 7 reports the bond lengths corrected by thermal factor according to the equation $R_{\text{SRB}}^2 = R^2 + (3/8\pi^2)[B_{\text{eq}}(Y) - B_{\text{eq}}(X)]$, where R_{SRB} is the length in the simple rigid-bond model correction, R is the uncorrected length, and $B_{\text{eq}}(X)$ and $B_{\text{eq}}(Y)$ are the isotropic equivalent temperature factors of the polyhedron central cation and the coordinated anions, respectively (Downs et al. 1992). Comparison of corrected and uncorrected bond lengths reveals that basal tetrahedral bond lengths are the ones most influenced by temperature factors, showing marked lengthening when the tetrahedral Fe³⁺ amount is maximum. This feature, according to Downs et al. (1992), shows that O1 and O2 thermal factors are significantly greater than the factors of the coordinated tetrahedral cation, whereas the variations in the other polyhedral bond lengths are much smaller.

Octahedral sheet. For most samples, the octahedral sites follow the homooctahedral type-I (Weiss et al. 1992) general trend of phlogopite. The mean bond lengths and distortions of both octahedra are quite similar (Fig. 3a) with the exception of crystals Tag15-3 and Tpg63-2B, which

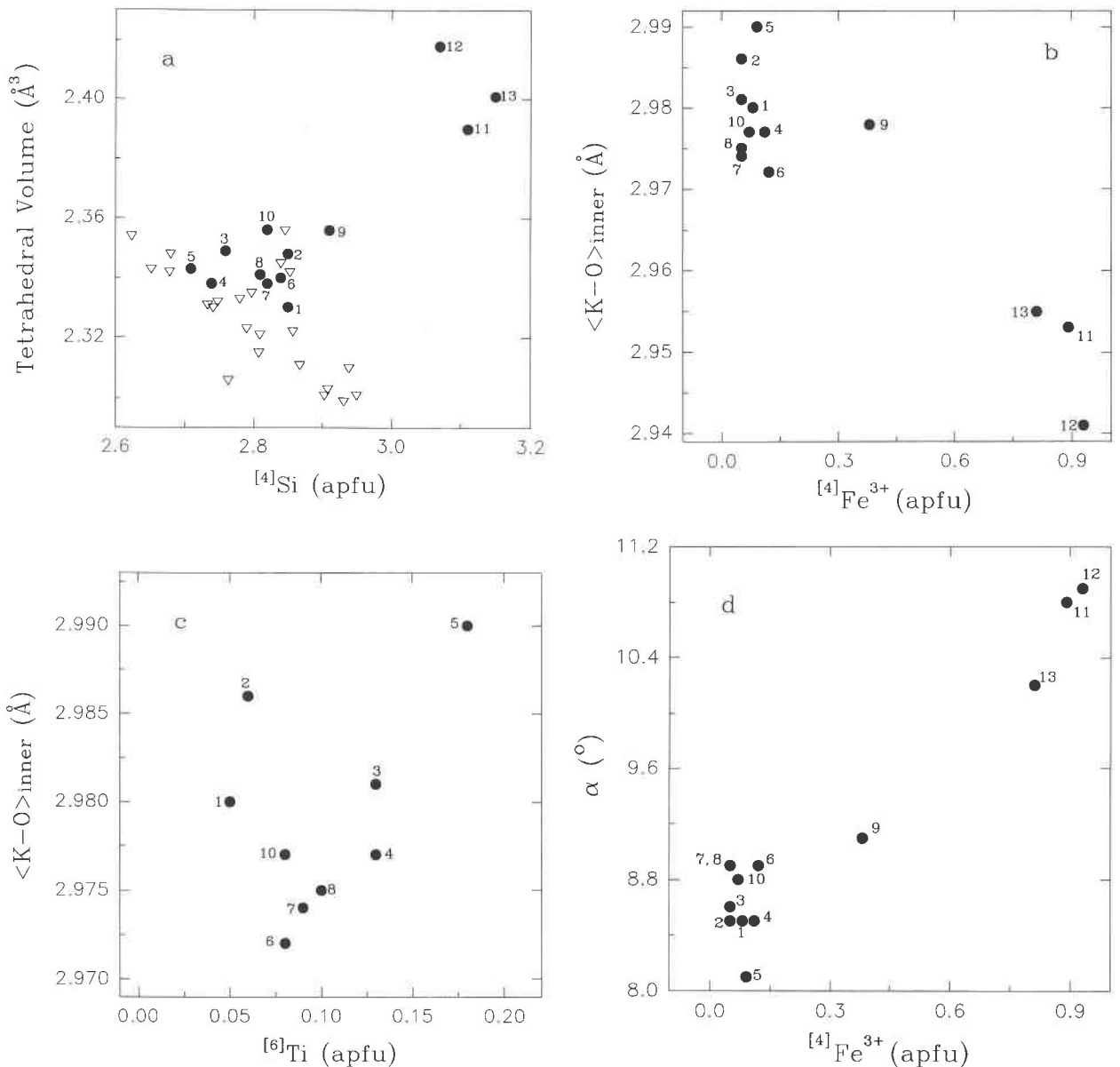


FIGURE 2. Diagrams of (a) tetrahedral volumes vs. [4]Si, (b) $\langle K-O \rangle_{\text{inner}}$ vs. [4]Fe³⁺, (c) $\langle K-O \rangle_{\text{inner}}$ vs. [6]Ti, and (d) tetrahedral angle ring distortion (α) vs. [4]Fe³⁺ for Tapira phlogopite and ferriphlogopite. Samples are as follows: 1 = Tas27-2Ba, 2 = Tas27-2Bb, 3 = Tag15-4, 4 = Tag15-3, 5 = Tpg63-2B, 6 = Tae23-1a, 7 = Tae23-1b, 8 = Tae23-1c, 9 = Tpq16-4A, 10 = Tpt17-1, 11 = Tas22-1a, 12 = Tas22-1b, 13 = Tpq16-6B. Dots = phlogopite and ferriphlogopite samples from this study, and open triangles = crystals in the phlogopite-annite join from the literature (Brigatti and Davoli 1990; Brigatti et al. 1991; Brigatti and Poppi 1993; Bigi and Brigatti 1994; Takeda and Ross 1975; Hazen and Burnham 1973; Joswig 1972).

show the normal ordering pattern for octahedral cations in micas (Bailey 1984), with volumes and flattening angles of the trans M1 site greater than those of the cis M2 site. Furthermore, in comparison with the previously studied crystals in the phlogopite-annite join, all samples exhibit octahedral mean bond lengths (especially for the M2 site) approaching the highest values, whereas octahedral distortion parameters tend toward the lowest values (Figs. 3b and 3c, Tables 6 and 8). These geometrical variations, together with an increase in the in-plane ro-

tation of adjacent tetrahedra (i.e., the α angle), are the main factors required to avoid lateral misfit between tetrahedral and octahedral sheets. This behavior is confirmed by the positive trend shown in Figure 3d, which compares $\langle M2-O \rangle$ mean bond lengths with the mean basal tetrahedral bond lengths ($\langle T-O \rangle_{\text{basal}}$).

Comparison of the Ti contents with the M2-O4 bond length reveals the close connection between the M2 cation off-center shift and Ti (Fig. 3e). This relationship is in agreement with that reported by Cruciani and Zanazzi

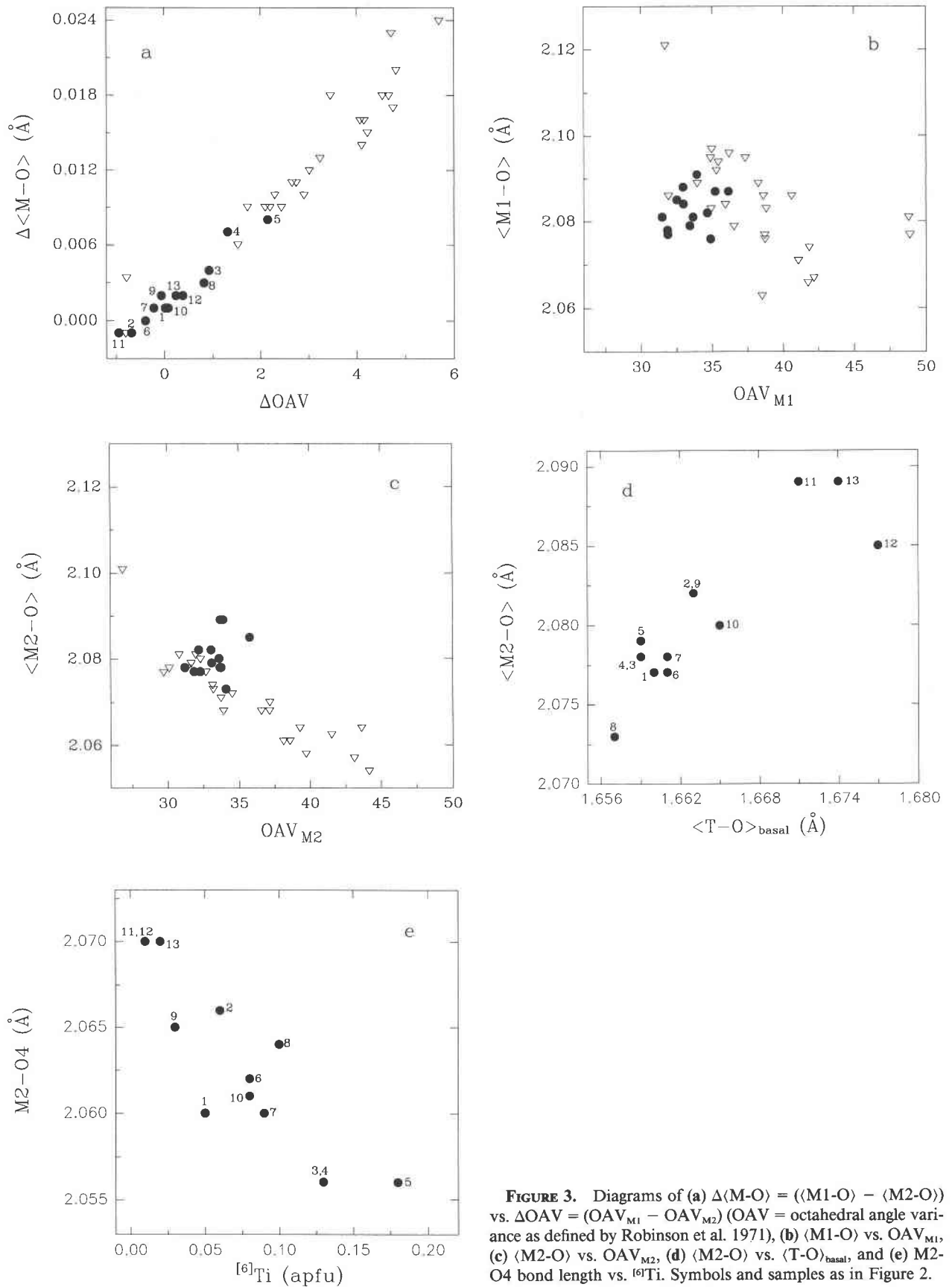


FIGURE 3. Diagrams of (a) $\Delta\langle M-O \rangle = (\langle M1-O \rangle - \langle M2-O \rangle)$ vs. $\Delta OAV = (OAV_{M1} - OAV_{M2})$ (OAV = octahedral angle variance as defined by Robinson et al. 1971), (b) $\langle M1-O \rangle$ vs. OAV_{M1} , (c) $\langle M2-O \rangle$ vs. OAV_{M2} , (d) $\langle M2-O \rangle$ vs. $\langle T-O \rangle_{\text{basal}}$, and (e) $M2-O4$ bond length vs. $[6]Ti$. Symbols and samples as in Figure 2.

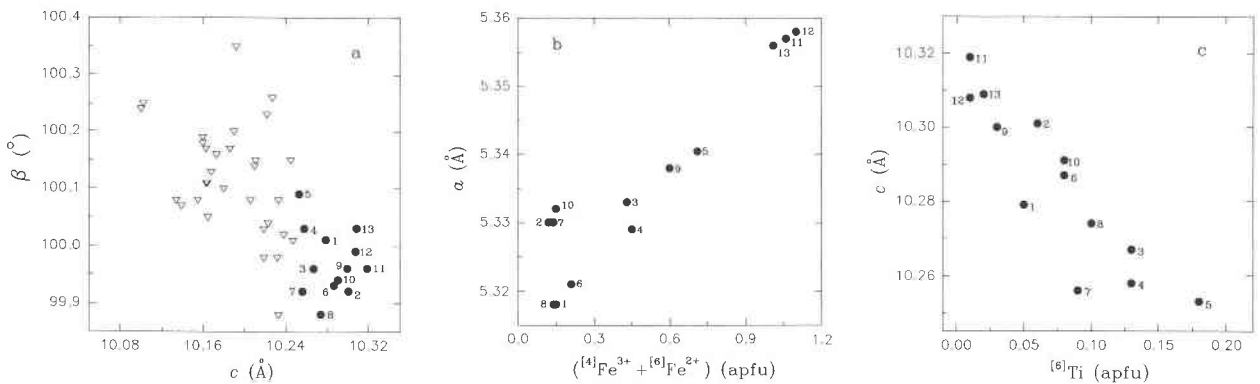


FIGURE 4. Diagrams of (a) β vs. c cell parameter, (b) a cell parameter vs. $(^{44}\text{Fe}^{3+} + ^{66}\text{Fe}^{2+})$, and (c) c cell parameter vs. ^{66}Ti . Symbols and samples as in Figure 2.

(1994), i.e., Ti cations in the octahedral M2 site are displaced from the geometric center of the octahedron, toward O4, along the twofold axis. Furthermore, the low Ti content of the $^{44}\text{Fe}^{3+}$ -rich samples is probably related to high tetrahedral charge.

In most samples, the O-H distance is in the range 0.90–1.15 Å, and the OH vector orientation is almost parallel to c^* . This feature confirms the observation reported by Bailey (1984): True trioctahedral micas, without octahedral vacancies, show the OH vector direction normal to the (001) plane.

In Fe³⁺-rich samples, small positive anomalies were found near the O4 atom in ΔF maps; nevertheless, their low intensity (4 above the background) does not allow an accurate localization.

Variation of cell parameters as a function of composition. The high values of cell volumes result from the lengthening of a , b , and c cell parameters (Table 4, Fig. 4a). The β angles are among the lowest found for 1M phlogopite ($99.88^\circ \leq \beta \leq 100.09^\circ$), and the ideal value [$\beta_{\text{ideal}} = \arccos(-a/3c)$; Bailey 1975, 1984] is nearly equal to that observed (Tables 4 and 8). The lateral dimensions a and b increase with the increasing contents of large cations such as $^{44}\text{Fe}^{3+}$ and $^{66}\text{Fe}^{2+}$ (Fig. 4b). The composition of the tetrahedral sheet exerts strong control on the lateral cell dimensions. The c parameter increases with increasing $^{44}\text{Fe}^{3+}$ and regularly decreases with ^{66}Ti content (Fig. 4c). As observed by Cruciani and Zanazzi (1994), reduction in c is linked to the decrease in the K-O4 distance, which can be produced by the Ti-oxy exchange vector [$^{66}\text{TiO}_2^{66}\text{Mg}_{-1}(\text{OH})_{-2}$]. Nevertheless, the presence of Ti vacancies and Ti Tschermak exchange vectors cannot be excluded.

Origin and crystallization of phlogopite from Tapira complex

Although a liquid line of descent is not represented by the rocks of the complex, which basically consist of cumulates, the various stages of phlogopite crystallization are evidently related to the fractional crystallization and

cumulus processes responsible for the generation of the rock sequence.

Because of the extreme peculiarity of the mineral assemblages forming the studied rocks (see Petrography section), the pressure, temperature, and f_{O_2} conditions under which phlogopite crystallized cannot be easily estimated by means of the common geothermobarometric calculations. However, several authors have noted that the different behaviors of Al, Fe³⁺, Ti, Mg, and Fe²⁺ can be related to a combination of factors such as temperature, pressure, f_{O_2} , and magma composition. In particular, Arima and Edgar (1981), in their research on phlogopite from peridotitic xenoliths and high-K rocks of mantle origin, reported the tendency of TiO₂ to increase with decreasing tetrahedral site occupancy by Al and Si, coupled with an increase of $^{44}\text{Fe}^{3+}$, which is related, in turn, to temperature and f_{O_2} increase and pressure decrease. These authors pointed out the scarce influence of bulk-rock composition on phlogopite chemistry. Barton (1979), on the other hand, observed the close relationship between Al₂O₃ content of phlogopite and the composition of the K-rich, alkaline host rocks. The influence of bulk-rock composition, as well as high H₂O activity ($a_{\text{H}_2\text{O}}$), has also been recognized on the basis of high-pressure experimental studies by Edgar and Arima (1983). Foley (1989, 1990) obtained experimental data on phlogopite chemistry in lamproite, showing that fluid composition (H₂O, CO₂, and CH₄) exerts much greater control on mica composition than do pressure, temperature, and bulk-rock chemistry. Nevertheless, he emphasized that mica substitutions in lamproite may differ from those in the experiments because of the predominance of crystal fractionation, pressure, and temperature effects over fluid composition. It is worth noting, however, that the results obtained by the above authors concern micas crystallized from petrologic systems notably different from the Tapira complex. In fact, all the phlogopite samples studied in this paper are characterized by Al + Si < 4 apfu (Fig. 1a). In addition, the presence of two distinct phlogopite types, which can be related to two basic genetic conditions, can be deduced from Figures 1a–1d:

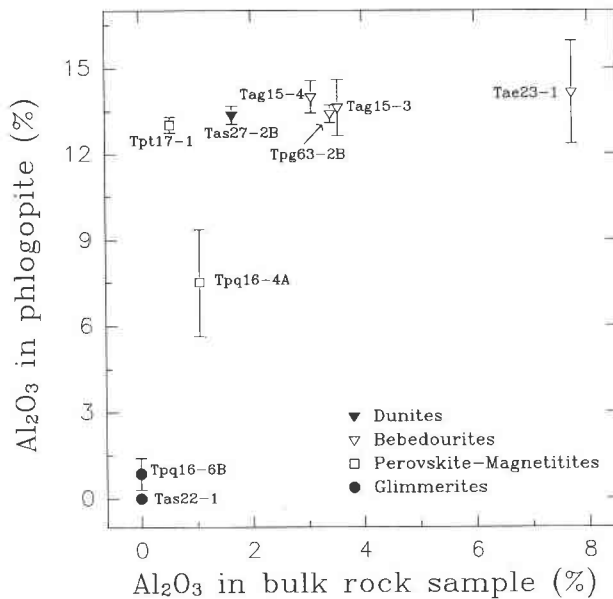


FIGURE 5. Diagrams of Al₂O₃ (wt%) in mineral vs. Al₂O₃ in bulk-rock sample for Tapira phlogopite and ferriphlogopite. Symbols represent the average compositions (with variance bars) of different analyzed crystals.

(1) Phlogopite crystallized from alkaline-silicate magmas (i.e., in dunite, wehrlite, clinopyroxenite, bebedourite, and garnet magnetite) shows relatively low ⁴¹Fe³⁺-for-⁴¹Al substitution (<0.3 apfu), coupled with a decrease in the Mg/(Mg + Fe²⁺) ratio (97.6 > Mg' > 90.8) and an increase in ⁶⁰Ti during fractional crystallization (Table 2). Crystals showing normal pleochroism prevail, although an increase in abundance of micas with reverse pleochroism from dunite to bebedourite can be recognized. Several considerations can be deduced from these features. (a) There is clear evidence of early crystallization of phlogopite as intercumulus. (b) The increasing TiO₂ content and the decreasing MgO and Mg' (Fig. 1e) during fractional crystallization reflect an increasing *f*_{O₂} in the liquid characterized by moderate saturation of Ti-bearing phases (perovskite, titaniferous magnetite ± schorlomite). Actually, Edgar and Arima (1983) showed that TiO₂ may be preferentially incorporated into phlogopite in the absence of Ti-bearing phases and that the solubility of TiO₂ in phlogopite is much more controlled by the presence of TiO₂ in the liquid than are coexisting Ti-bearing phases. Moreover, Arima and Edgar (1981) and Foley (1990) noted that the solubility of Ti in phlogopite increases with increasing *f*_{O₂} and CO₂ in the liquid, which, in turn, is related to fractional crystallization. Foley (1990) concluded that the exchange vector ⁶⁰Ti⁶⁺□⁶⁺Mg₂ in phlogopite is an important substitution mechanism in CO₂-bearing oxidized melts. This can explain the decreasing Mg' and increasing TiO₂ in phlogopite (Fig. 1a). (c) The deficiency of Al in the tetrahedral site can presumably be related to a predominance of the effect of *f*_{O₂} over bulk composition (namely, Al₂O₃ con-

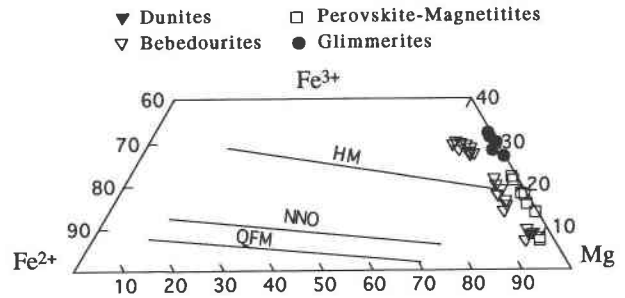


FIGURE 6. Tapira phlogopite and ferriphlogopite composition in terms of Fe³⁺, Fe²⁺, and Mg. The *f*_{O₂} buffer limits are from Wones and Eugster (1965).

tent in the magma). Actually, from Figure 5 it can be observed that Al₂O₃ in micas is quite constant, indicating an adequate availability of this element in the system. Thus, the increasing ⁴¹Fe³⁺-for-⁴¹Al substitution can be mainly accounted for by an increase of Fe³⁺ in the liquid.

(2) In silicate-carbonatite rocks (perovskite magnetite, glimmerite, and carbonatite) phlogopite is the only silicate phase and shows marked reverse pleochroism, very high ⁴¹Fe³⁺-for-⁴¹Al substitution (0.1–1.0 apfu) and Mg' (100–97.1), and low Ti content. Such characteristics, together with textural features, seem to account for a fractional crystallization from a liquid strongly saturated with Ti-bearing phases (perovskite, titaniferous magnetite, and schorlomite) in a very high *f*_{O₂}, *a*_{H₂O}, and *a*_{CO₂} system. The relationship TiO_{2(phl)} < TiO_{2(Ti-m)} < TiO_{2(pv)} controls the TiO₂ partitioning in phlogopite, in spite of the high *f*_{O₂} and TiO₂ availability in the liquid (Edgar and Arima 1983). The high Mg' in phlogopite is mainly related to the high *f*_{O₂}, which produces Fe²⁺ → Fe³⁺ transformation combined with the contemporaneous crystallization of magnetite [assuming that FeO_(phl) ≪ FeO_(m)]. According to Barton (1979), the low to very low Al₂O₃ content (12.69–0.00 wt%) in micas is closely related to the scarcity of this element in silicate-carbonatite magmas.

Pressure conditions cannot be directly estimated from mineral assemblages; however, field relationships and textural features suggest that the Tapira plutonic complex crystallized at a high crustal level (few kilometers in depth) and high cooling rate, analogous to other alkaline-carbonatite plutonic complexes of Brazil (Beccaluva et al. 1992). This low crystallization depth could explain, for some samples, the lack of ordering of Fe²⁺ and Mg between M1 and M2 octahedral sites (Tables 3 and 6). Otherwise, a low cooling rate may induce Fe²⁺ occupancy of the M1 site.

In conclusion, the crystallization of Tapira complex mineral assemblages indicates *f*_{O₂} conditions above the NNO buffer (Fig. 6), which is consistent with alkaline magmas derived from strongly metasomatized mantle (Beccaluva et al. 1992; Siena and Coltorti 1993). In addition, hematitic rims around phlogopite in glimmerite indicate that tardo-magmatic oxidizing processes cannot be excluded.

ACKNOWLEDGMENTS

We are particularly grateful to L. Beccaluva (Ferrara University), E. Galli and L. Poppi (Modena University), and F. Siena (Catania University) for their precious help and critical review of the manuscript. M. Coltorti is thanked for XRF analyses. We are much obliged to the reviewers, A. Lalonde, A.E. Patino-Douce, and D. Rancourt, whose comments greatly improved the paper. The authors are grateful to L. Bruce for the English review. This work was supported by Ministero dell'Università e della Ricerca Scientifica (MURST) and by Consiglio Nazionale delle Ricerche (CNR) of Italy. The Consiglio Nazionale delle Ricerche is also acknowledged for financing the Electron Microprobe Laboratory at Modena University.

REFERENCES CITED

- Arima, M., and Edgar, A.D. (1981) Substitution mechanism and solubility of titanium in phlogopites from rocks of probable mantle origin. *Contributions to Mineralogy and Petrology*, 77, 288–295.
- Bailey, S.W. (1975) Cation ordering and pseudosymmetry in layer silicates. *American Mineralogist*, 60, 175–187.
- (1984) Crystal chemistry of the true micas. In *Mineralogical Society of America Reviews in Mineralogy*, 13, 13–60.
- (1988) X-ray diffraction identification of the polytypes of mica, serpentine, and chlorite. *Clays and Clay Minerals*, 36, 195–213.
- Barton, M. (1979) A comparative study of some minerals occurring in the potassium-rich alkaline rocks of the Leucite Hills, Wyoming, the Vico Volcano, Western Italy, and the Toro-Ankole Region, Uganda. *Neues Jahrbuch für Mineralogie Abhandlungen*, 137, 113–134.
- Beccaluva, L., Barbieri, M., Born, H., Brotzu, P., Coltorti, M., Conte, A., Garbarino, C., Gomes, C.B., Macciotta, G., Morbidelli, L., Ruberti, E., Siena, F., and Traversa, G. (1992) Fractional crystallization and liquid immiscibility processes in the Alkaline-Carbonatite Complex of Juquiá (Sao Paulo, Brazil). *Journal of Petrology*, 33, 1371–1404.
- Beurlen, H., and Cassadanne, J.P. (1981) The Brazilian mineral resources. *Earth Sciences Review*, 17, 177–206.
- Bigi, S., and Brigatti, M.F. (1994) Crystal chemistry and microstructures of plutonic biotite. *American Mineralogist*, 79, 63–72.
- Brigatti, M.F., and Davoli, P. (1990) Crystal-structure refinement of 1M plutonic biotites. *American Mineralogist*, 75, 305–313.
- Brigatti, M.F., Galli, E., and Poppi, L. (1991) Effect of Ti substitution in biotite-1M crystal chemistry. *American Mineralogist*, 76, 1174–1183.
- Brigatti, M.F., and Poppi, L. (1993) Crystal chemistry of Ba-rich trioctahedral micas 1M. *European Journal of Mineralogy*, 5, 857–871.
- Busing, W.R., Martin, K.O., and Levi, H.S. (1962) ORFLS, a Fortran crystallographic least-square program. U.S. National Technical Information Service ORNL-TM-305.
- Cruciani, G., and Quartieri, S. (1992) XANES investigation on iron in phlogopites-1M: First results and perspectives. *Proceedings of the Italian National School on Synchrotron Light and Chemical Research*, Cagliari, 1–4.
- Cruciani, G., and Zanazzi, P.F. (1992) Phlogopite from mantle derived rocks: Fe³⁺ in tetrahedral coordination. *Proceedings of the Italian Association of Crystallography, L'Aquila*, 114–115.
- (1994) Cation partitioning and substitution mechanisms in 1M-phlogopite: A crystal chemical study. *American Mineralogist*, 78, 289–301.
- Donnay, G., Morimoto, N., Takeda, H., and Donnay, D.H. (1964) Trioctahedral one-layer micas: 1. Crystal structure of a synthetic iron mica. *Acta Crystallographica*, 17, 1369–1373.
- Downs, R.T., Gibbs, G.V., Bartelmehs, K.L., and Boisen, M.B., Jr. (1992) Variations of bond lengths and volumes of silicate tetrahedra with temperature. *American Mineralogist*, 77, 751–757.
- Dyar, M.D. (1990) Mössbauer spectra of biotite from metapelites. *American Mineralogist*, 75, 656–666.
- Dymek, R.F. (1983) Titanium, aluminum and interlayer cation substitutions in biotite from high-grade gneisses, West Greenland. *American Mineralogist*, 68, 880–899.
- Edgar, A.D., and Arima, M. (1983) Conditions of phlogopite crystallizations in ultrapotassic volcanic rocks. *Mineralogical Magazine*, 47, 11–19.
- Farmer, L.G., and Boettcher, A.L. (1981) Petrologic and crystal chemical significance of some deep-seated phlogopites. *American Mineralogist*, 66, 1154–1163.
- Foley, S.F. (1989) Experimental constraints on phlogopite chemistry in lamproites: 1. The effect of water activity and oxygen fugacity. *European Journal of Mineralogy*, 1, 411–426.
- (1990) Experimental constraints on phlogopite chemistry in lamproites: 2. The effect of pressure-temperature variations. *European Journal of Mineralogy*, 2, 327–341.
- Franzini, M., Leoni, L., and Saitta, M. (1975) Revisione di una metodologia analitica per fluorescenza-X, basata sulla correzione completa degli effetti di matrice. *Rendiconti della Società Italiana di Mineralogia e Petrologia*, 31, 635–678.
- Gaspar, J.C., and Wyllie, P.J. (1982) Barium phlogopite from the Jacupiranga carbonatite, Brazil. *American Mineralogist*, 67, 997–1000.
- Guidotti, C.V., and Dyar, M.D. (1991) Ferric iron in metamorphic biotites and its petrologic and crystallochemical implications. *American Mineralogist*, 76, 161–175.
- Hasui, Y., and Cordani, U.G. (1968) Idades Potássio-argonio de Rochas Eruptivas Mesozóicas do Oeste Mineiro e Sul de Goiás. In *XXII Congresso Brasileiro de Geologia*, Belo Horizonte, 139–143.
- Hazen, R.M., and Burnham, C.W. (1973) The crystal structures of one-layer phlogopite and annite. *American Mineralogist*, 58, 889–900.
- Hazen, R.M., Finger, L.W., and Velde, D. (1981) Crystal structure of a silica- and alkali-rich trioctahedral mica. *American Mineralogist*, 66, 586–591.
- Herz, N. (1977) Timing of spreading in the South Atlantic: Information from Brazilian alkaline rocks. *Geological Society of America Bulletin*, 88, 101–112.
- Jackson, M.L. (1958) *Soil chemical analysis*, 498 P. Prentice-Hall, New York.
- Jakob, J. (1925) X. beiträge zur chemischen konstitution der glimmer. I. Mitteilung die schwedischen manganophylle. *Zeitschrift für Kristallographie*, 61, 155–163.
- Johannsen, A. (1951) *A descriptive petrography of the igneous rocks* (vol. IV), 523 p. University of Chicago Press, Chicago, Illinois.
- Joswig, W. (1972) Neutronenbeugungsmessungen an einem 1M-phlogopit. *Neues Jahrbuch für Mineralogie Monatshefte*, 1–11.
- Leoni, L., and Saitta, M. (1976) X-ray fluorescence analysis of 29 trace elements in rock and mineral standards. *Rendiconti della Società Italiana di Mineralogia e Petrologia*, 32, 497–510.
- Lipson, H., and Cochran, W. (1953) *The crystalline state: Vol. III. The determination of crystal structures*. Bell and Sons, London, U.K.
- Meyrowitz, R. (1970) New semimicroprocedure for determination of ferrous iron in refractory silicate minerals using a sodium metafluoborate decomposition. *Analytical Chemistry*, 42, 1110–1113.
- Neal, C.R., and Taylor, L.A. (1989) The petrography and composition of phlogopite micas from the Blue Ball kimberlite, Arkansas: A record of chemical evolution during crystallization. *Mineralogy and Petrology*, 40, 207–224.
- Ohta, T., Takeda, H., and Takéuchi, Y. (1982) Mica polytypism: Similarities in the crystal structures of coexisting 1M and 2M₁ oxybiotite. *American Mineralogist*, 67, 298–310.
- Rancourt, D.G., Dang, M.Z., and Lalonde, A.E. (1992) Mössbauer spectroscopy of tetrahedral Fe³⁺ in trioctahedral micas. *American Mineralogist*, 77, 34–93.
- Robinson, K., Gibbs, G.V., and Ribbe, P.H. (1971) Quadratic elongation: A quantitative measure of distortion in coordination polyhedra. *Science*, 172, 567–570.
- Semenova, T.F., Rozhdestvenskaya, I.V., and Frank-Kamenetskii, V.A. (1977) Refinement of crystal structure of tetraferriphlogopite. *Soviet Physics Crystallography*, 22, 680–683.
- Semenova, T.F., Rozhdestvenskaya, I.V., Frank-Kamenetskii, V.A., and Pavlishin, V.I. (1983) Crystal structure of tetraferriphlogopite and tetraferribiotite. *Mineralogical Journal*, 5, 41–49.
- Siena, F., and Coltorti, M. (1993) Thermobarometric evolution and metasomatic processes of upper mantle in different tectonic settings: Evi-

- dence from spinel peridotite xenoliths. *European Journal of Mineralogy*, 5, 1073–1090.
- Steinfink, H. (1962) Crystal structure of a trioctahedral mica phlogopite. *American Mineralogist*, 47, 886–896.
- Takeda, H., and Ross, M. (1975) Mica polytypism: Dissimilarities in the crystal structures of coexisting $1M$ and $2M_1$ biotite. *American Mineralogist*, 60, 1030–1040.
- Toraya, H. (1981) Distorsions of octahedra and octahedral sheets in $1M$ micas and the relation to their stability. *Zeitschrift für Kristallographie*, 157, 173–190.
- Ulbrich, H.H.G.J., and Gomes, C.B. (1981) Alkaline rocks from continental Brazil. *Earth Sciences Review*, 17, 135–154.
- Weiss, Z., Rieder, M., and Chmielova, M. (1992) Deformation of coordination polyhedra and their sheets in phyllosilicates. *European Journal of Mineralogy*, 4, 665–682.
- Wones, D.R., and Eugster, H.P. (1965) Stability of biotite: Experiments, theory, and application. *American Mineralogist*, 50, 1228–1272.

MANUSCRIPT RECEIVED JUNE 26, 1995

MANUSCRIPT ACCEPTED FEBRUARY 27, 1996